



Universiteit
Leiden
The Netherlands

The electrode-electrolyte interface in CO₂ reduction and H₂ evolution: a multiscale approach

Cecilio de Oliveira Monteiro, M

Citation

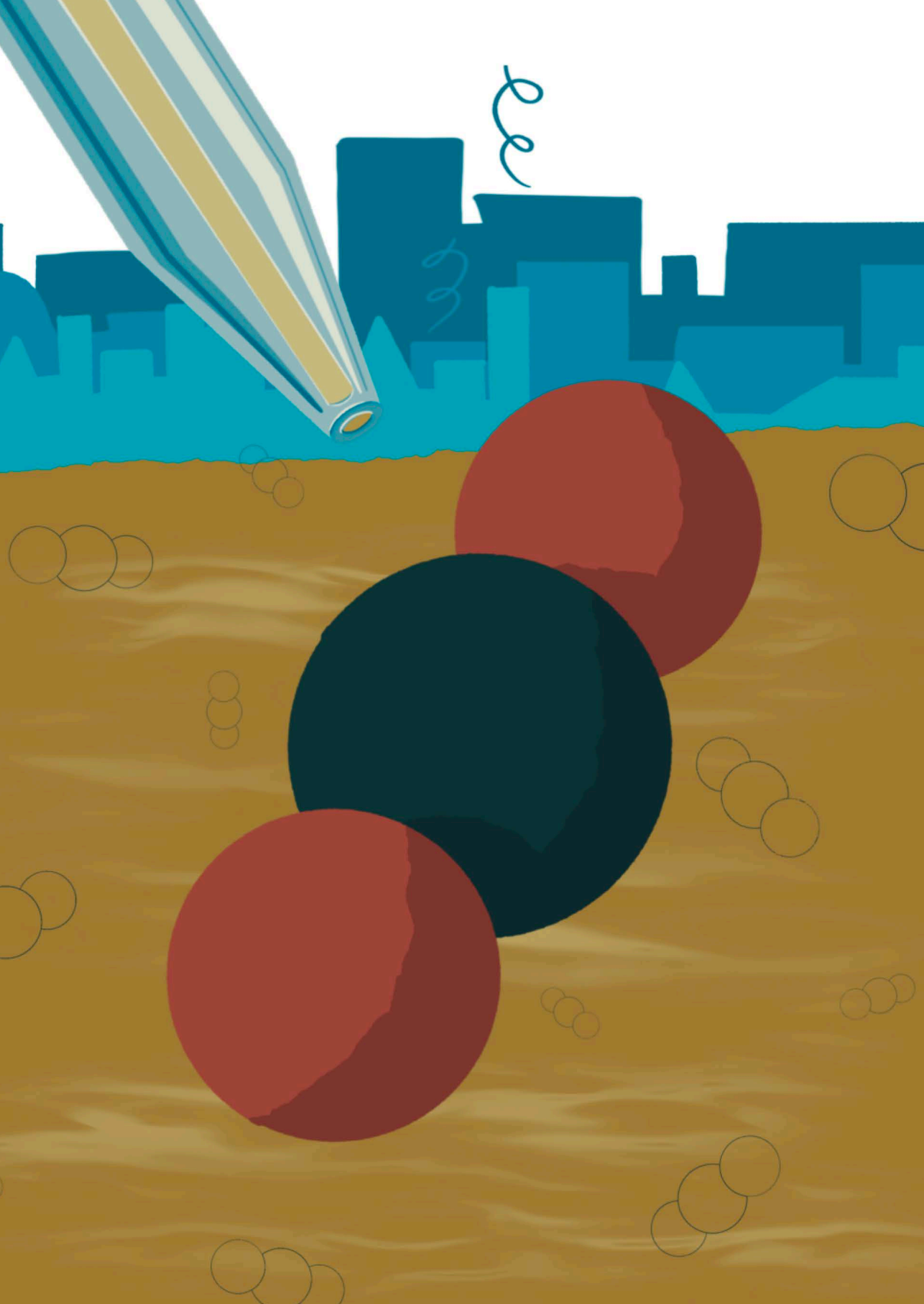
Cecilio de Oliveira Monteiro, M. (2022, February 15). *The electrode-electrolyte interface in CO₂ reduction and H₂ evolution: a multiscale approach*. Retrieved from <https://hdl.handle.net/1887/3274033>

Version: Publisher's Version

License: [Licence agreement concerning inclusion of doctoral thesis in the Institutional Repository of the University of Leiden](#)

Downloaded from: <https://hdl.handle.net/1887/3274033>

Note: To cite this publication please use the final published version (if applicable).



A stylized illustration of a city skyline in light blue and white, with a large blue number '4' in the upper right corner. A white squiggly line resembling a plume of smoke or steam rises from one of the buildings.

4

Time-resolved local pH measurements during CO₂ reduction using SECM: buffering and tip effects

This chapter is based on Monteiro, M. C. O., Mirabal, A., Jacobse, L., Doblhoff-Dier, K., Barton, S. C., Koper, M. T. M. *JACS Au*, 1 (11), 1915–1924 (2021)

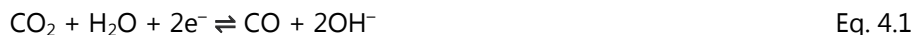
Abstract

The electrochemical reduction of CO_2 is widely studied as a sustainable alternative to produce fuels and chemicals. The electrolyte's bulk pH and composition play an important role in the reaction activity and selectivity, and can affect the extent of the build-up of pH gradients between the electrode surface and the bulk of the electrolyte. Quantifying the local pH and how it is affected by the solution species is desirable to gain a better understanding of the CO_2 reduction reaction. Local pH measurements can be realized using Scanning Electrochemical Microscopy (SECM), however, finding a pH probe that is stable and selective under CO_2 reduction reaction conditions is challenging. Here, we have used our recently developed voltammetric pH sensor to perform pH measurements in the diffusion layer during CO_2 reduction using SECM, with high time resolution. Using a 4-hydroxylaminothiophenol (4-HATP)/4-nitrosothiophenol (4-NSTP) functionalized gold ultramicroelectrode, we compare the local pH developed above a gold substrate in an argon atmosphere, when only hydrogen evolution is taking place, to the pH developed in a CO_2 atmosphere. The pH is monitored at a fixed distance from the surface, and the sample potential is varied in time. In argon, we observe a gradual increase of pH, while a plateau region is present in CO_2 atmosphere due to the formation of HCO_3^- buffering the reaction interface. By analysing the diffusion layer dynamics once the sample reaction is turned "off", we gain insightful information on the time scale of the homogeneous reactions happening in solution and on the time required for the diffusion layer to fully recover to the initial bulk concentration of species. To account for the effect of the presence of the SECM tip on the measured pH, we performed Finite Element Method simulations of the fluid and reaction dynamics. The results show the significant localized diffusion hindrance caused by the tip, so that in its absence the pH values are more acidic than when the tip is present. Nonetheless, through the simulation we can account for this effect and estimate the real local pH values across the diffusion layer.

4.1 Introduction

The electrochemical conversion of CO₂ to higher added value products has gained attention in the past years as a potential pathway towards replacing fossil fuels as feedstock. In aqueous media, the reduction of CO₂ (CO₂RR) competes with the hydrogen evolution reaction (HER), and activity and selectivity are key factors to make this process viable at industrially relevant scales.¹ In order to steer the selectivity and improve the overall reaction energetics, most studies focus on the catalyst material.^{2,3} However, another efficient way of tuning CO₂RR is through the electrolyte composition.^{4,5} By changing the electrolyte's buffer capacity⁶⁻⁸, pH⁹⁻¹¹, cation¹²⁻¹⁵ or anion^{16,17} one can strongly influence the rate and selectivity of the reaction. However, understanding and decoupling these electrolyte effects is necessary in order to optimize the reaction via these variables.

In many studies, the activity for CO₂ reduction is assessed without actual knowledge of the interfacial pH, which can vary drastically from the bulk depending on the current density, electrolyte buffer capacity, and diffusion coefficient of the species in solution. On gold, at low overpotentials, CO₂RR and HER yield mainly carbon monoxide (CO) and hydrogen (H₂) through the following reactions:¹⁸



The interfacial pH and the overpotential will determine whether the overall HER current is dominated by proton or water reduction, displayed in Eq. 2 and 3, respectively. Because of the consumption of protons or formation of OH⁻ by both HER and CO₂RR, the pH near the electrode surface can drastically vary from the bulk pH. Apart from the reactions 4.1 to 4.3, various homogeneous reactions may take place in the CO₂-water system as a function of pH:¹⁹



Quantifying the pH gradients formed in the diffusion layer during CO₂RR is crucial in order to gain a better understanding of the reaction. Though various techniques are available for measuring local pH in electrochemistry²⁰ (Chapter 2), directly measuring the pH in the diffusion layer during CO₂ reduction is challenging. This is

due to the complex reaction environment, and the fact that, the signal and stability of the pH probe should not be affected by the reactants, products, or the electrolyte identity. To date, pH measurements during CO₂ reduction under stationary conditions have been mainly achieved using spectroscopic techniques. Yang et al.²¹, for instance, used surface enhanced infrared absorption spectroscopy (SEIRAS) to determine the pH near the surface during CO₂RR on sputtered copper thin films by monitoring the change in signal intensity of the species composing the phosphate buffer used (H₂PO₄⁻/ HPO₄²⁻/ PO₄³⁻). Results showed that even in strongly buffered electrolyte, the pH near the surface differs from the bulk at current densities lower than 10 mA cm⁻². Ayemoba et al.²² probed the pH during CO₂RR on gold thin films using surface-enhanced infrared absorption spectroscopy in the attenuated total reflection mode (ATR-SEIRAS). In this case, the ratio between the integrated absorbance of the CO₂ and HCO₃⁻ bands was used to estimate the pH near the surface. Similar measurements, were recently reported in a flow cell using Raman spectroscopy.²³ Although, in general, these spectroscopic techniques can provide valuable information about the concentration of species in the first few nanometres above the surface, the signal obtained is averaged over a large surface area. Furthermore, these measurements require having infrared or Raman active species in solution, and the pH is measured indirectly, by monitoring species whose signal is a function of the proton concentration. If these species are also affected by other variables of the reaction environment, the signal might be a convolution thereof. Therefore, spectroscopic techniques can be limited in terms of electrode materials and electrolytes that can be employed. As an alternative to spectroscopy, Zhang et al.²⁴ have recently used the rotating ring-disc electrode technique to measure changes in pH during CO₂RR on gold under mass transport control. In this case, a correlation between potentiometric pH measurements with IrO_x and shifts in the CO oxidation peak detected with a Pt ring were used to determine the disc pH. Even though this allows for pH measurements under mass transport control, the method is limited in terms of temporal (when IrO_x is used) and spatial resolution (similarly to spectroscopic techniques). Additionally, even though the CO signal on platinum is used as pH probe, it is known that this reaction is not only affected by pH²⁵, but also cation identity²⁶ or surface structure.²⁷

Scanning Electrochemical Microscopy (SECM) allows for performing pH measurements with high spatial and temporal resolution. The spatial resolution is only limited by the tip size and the temporal resolution depends on the pH probe used. SECM also offers a high versatility in terms of substrate (gas diffusion, flat,

thin film electrodes) and pH sensors (potentiometric, voltammetric) that can be used. However, finding a pH probe that is not destabilized by the CO₂ reduction reaction environment can be challenging. For example, commonly used (in both SECM and RRDE) potentiometric pH sensors such as IrO_x or Pt can strongly interact with CO. This can generate a convoluted open circuit potential response, hindering the applicability of these materials to measure pH during CO₂RR. Using gas diffusion electrodes (GDEs) operating at high current densities, Dieckenhöfer et al.²⁸ overcame this problem by collecting the products at the back of the GDE, so as to avoid CO getting in contact with the SECM Pt tip. Unfortunately, the pH response of the platinum nanoelectrode is only applicable in highly alkaline environments, as evident from the calibration curve reported by the authors in 1 to 16 M KOH solutions. Such a high alkalinity at the interface can only be achieved when using high turnover substrates (highly porous electrodes, GDEs) or when operating at high overpotentials. This means that this Pt sensor cannot be used to investigate CO₂RR on less porous substrates, or in neutral/acidic conditions. With that in mind, we have recently developed a highly stable, selective and sensitive SECM pH probe based on the functionalization of gold ultramicroelectrodes (Au-UMEs) with a 4-nitrothiophenol self-assembled monolayer.²⁹ Contrary to the commonly used IrO_x, this voltammetric pH probe can provide high temporal resolution, only dependent on the scan rate applied at the tip, showing a stable pH response in a wide pH range. Additionally, the fact that the sensor is formed by a monolayer on the tip surface, overcomes time response issues often encountered when using either a polymer or solid oxide film.

Our modified Au-UME pH sensor presented in Chapter 3, is employed in this work to perform and compare direct pH measurements during HER and CO₂RR on polycrystalline gold. We monitor the evolution of pH in time while stepping the electrode potential in either argon or CO₂ atmosphere. Our results show that the homogeneous reactions involving CO₂ in aqueous media are sufficient to buffer the reaction interface to a certain extent, in spite of using an otherwise unbuffered electrolyte. The high sensitivity and time resolution of our pH probe enables us to analyse the dynamics of the diffusion layer pH as a function of the species present in solution, which has not been previously reported for CO₂ reduction using SECM. Additionally, in this work we have accounted for the effect of the SECM tip on the diffusion layer concentration fields, and consequently on the pH measured for CO₂RR and HER, using 2D, dynamic transport and reaction simulations based on Finite Element Methods (FEM). Simulations are fitted to experimental results to

estimate kinetic parameters and enable further analysis of SECM tip effects relevant to the experimental system. This work brings pH measurements during CO₂RR one step further, by showing that it can be realized using SECM, with high time resolution and over a wide pH range. In future studies, this would allow for decoupling pH effects from other electrolyte/surface effects on the reaction.

4.2 pH sensor synthesis and calibration

The gold ultramicroelectrodes (Au-UMEs) are first characterized by blank voltammetry in 0.1 M H₂SO₄ in order to assure good sealing and surface cleanliness. A cyclic voltammogram characterizing the Au-UME (25 μm radius) used in this study can be seen in Fig. A.9 in Appendix A. To perform the SECM pH measurements, the Au-UME is functionalized with the 4-hydroxylaminothiophenol/4-nitrosothiophenol redox couple. This is done by immersion of the Au-UME in a solution containing 4-nitrothiophenol (4-NTP) which leads to the self-assembly of this organic molecule on the Au-UME surface. Next, 4-NTP is partially³⁰ electrochemically reduced to 4-hydroxylaminothiophenol (4-HATP) in 0.1 M H₂SO₄, as depicted in Fig. 4.1a. The cathodic potential limit must be carefully controlled in order to maximise the conversion to 4-HATP and minimise the amount of 4-aminothiophenol (4-ATP) formed. On the positive-going scan, an anodic peak can be seen in the gold double layer region between 0.2 and 0.4 V vs. Ag/AgCl due to oxidation of 4-HATP, forming 4-nitrosothiophenol (4-NSTP). This is a highly reversible reaction, demonstrated by the subsequent symmetrical cathodic current in the negative-going scan. A schematic representation of the reactions taking place at the Au-UME surface can be seen in the inset of Fig. 4.1a, which is correlated to the voltammetry of (1) the reduction of 4-NTP to 4-HATP and (2) the 4-HATP/4-NSTP redox couple.

The calibration of the functionalized Au-UME pH sensor is performed in the same electrolyte the SECM measurements are carried out, but in different gaseous atmospheres. The cyclic voltammetry (CV) of the tip is recorded in 0.1 M Li₂SO₄ solutions adjusted to different pH and saturated with either argon or CO₂. The CVs obtained in argon are shown in Fig. 4.1b and the ones recorded in CO₂ saturated electrolyte can be found in Fig. A.10 in Appendix A. The mid-peak potential of the 4-HATP/4-NSTP anodic voltammetry is obtained through a Gaussian fit (with a linear background) of the CVs, and can be used to construct the calibration curve shown in Fig. 4.1c. Due to the reversible oxidation and reduction of the 4-HATP/4-NSTP involving two protons and two electrons, a Nernstian response is obtained

with a shift of 57 mV/pH unit and an R^2 of 0.99. The calibration curves in argon and CO₂ atmosphere overlap until pH 3.45. This is expected as at higher pH values, carbonic acid is formed and the CO₂ saturated solutions equilibrate at a constant pH around 4 (see Eq. 4.4 and 4.5). We have also displayed the calibration

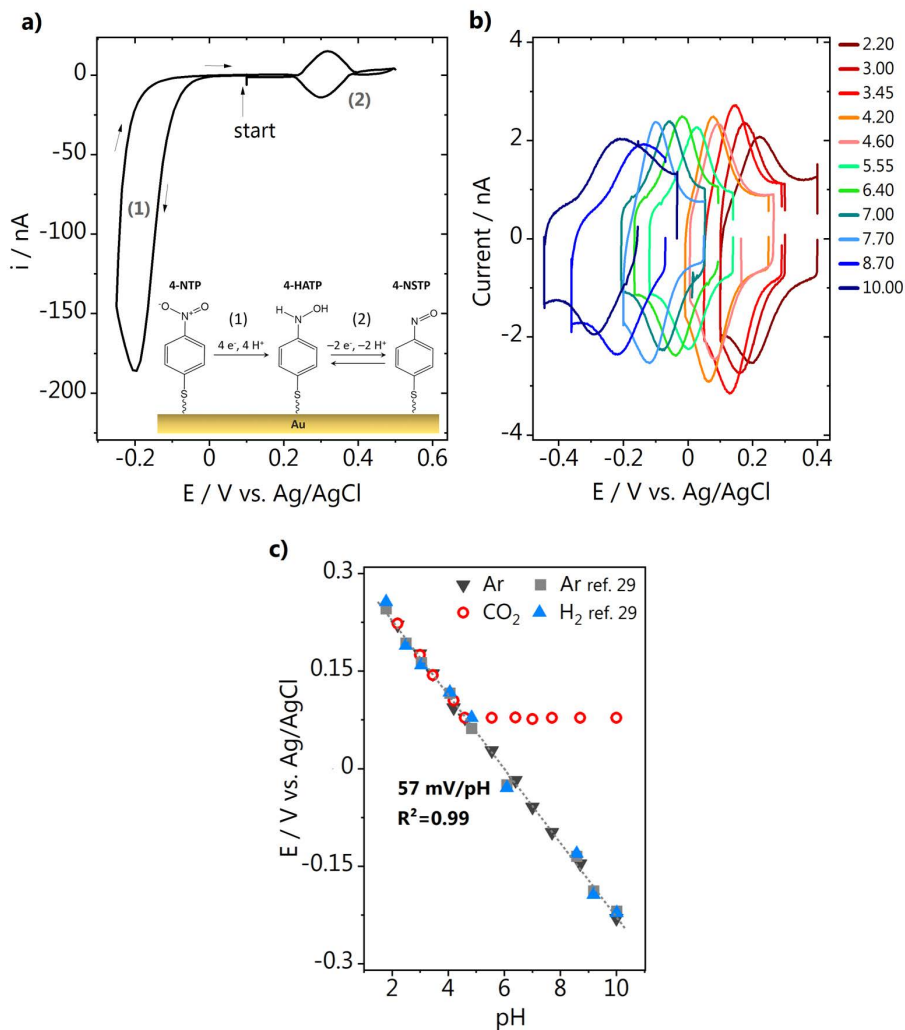


Fig. 4.1. SECM pH sensor synthesis and calibration. **a)** voltammogram of the functionalized Au-UME showing the conversion of 4-nitrothiophenol (4-NTP) to the pH sensitive redox couple 4-hydroxylaminothiophenol (4-HATP)/4-nitrosothiophenol(4-NTP); **b)** pH sensor voltammetry in 0.1 M Li₂SO₄ solutions adjusted to different pH, taken at 200 mV s⁻¹; **c)** calibration curves of the modified Au-UME pH sensor in different gaseous atmospheres. The calibration curves from our previous work (Chapter 3, Ref. 29) are also shown for comparison.

curves presented in Chapter 3²⁹ in Fig. 4.1c, which show how reproducible the pH sensor response is when comparing different measurements, performed in different gaseous atmospheres.

4.3 SECM measurements

Once the Au-UME is functionalized, the tip is positioned at a certain distance to the sample using a capacitive approach in air, which was introduced in our previous work (Chapter 3).^{25,29,31} In short: an AC potential is applied to the sample while the capacitive current generated at the tip is recorded. The capacitance is plotted as a function of distance from the surface (Fig. A.11), and behaves exponentially at small tip-to-surface distances. The fitting of the approach curve (see Chapter 3) is used to determine the absolute surface position. Before performing the SECM pH measurements, the cyclic voltammetry of HER and CO₂RR taking place at the polycrystalline gold sample in 0.1 M Li₂SO₄ (pH_{bulk} = 3) was recorded (Fig. 4.2). In argon atmosphere a large cathodic current is observed at potentials more negative than -0.4 V vs. Ag/AgCl due to the reduction of protons. The reaction becomes diffusion limited due to the depletion of protons at the interface and consequently in the subsequent four cycles a significantly lower proton reduction current is observed. In the presence of CO₂, proton reduction and CO₂ reduction take place in parallel, but a larger current is observed only at potentials more negative than -1 V vs. Ag/AgCl, suggesting that the contribution of CO₂ reduction to the current observed at more positive potentials is minimal. The first cycle overlaps with the CV taken in argon atmosphere, as the starting bulk pH is the same, however larger currents are obtained in the subsequent four cycles in CO₂ atmosphere. The latter indicates that the alkalinity near surface is lower in the presence of CO₂. However, cyclic voltammetry can only provide qualitative information about the proton concentration near the surface.

To quantify the changes in pH in the diffusion layer during these reactions using SECM, the functionalized Au-UME pH sensor is placed at a constant distance of $80 \pm 2 \mu\text{m}$ from the gold surface. Similarly to Chapter 3, the reactions are turned "on" and "off" by stepping the sample potential from -0.5 to -0.9 V vs. Ag/AgCl in 50 mV steps. In between potential steps, the gold substrate is held at 0 V. The tip voltammetry is constantly recorded at 200 mV s^{-1} , which allows capturing the changes in pH with high time resolution (4 seconds/data point). Fig. 4.3a shows the results obtained in argon atmosphere (gray triangles) and then in CO₂ atmosphere (red circles). These data were obtained in two consecutive measurements and are

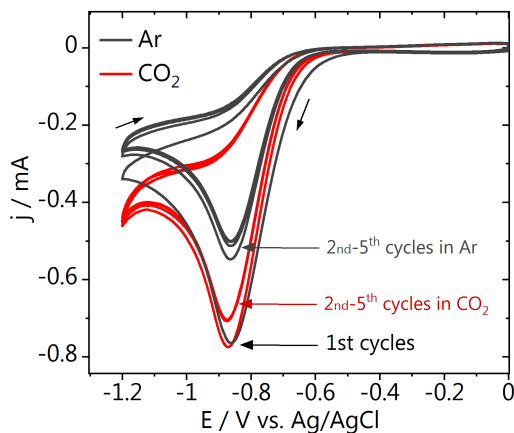


Fig. 4.2. CVs in argon (black) and CO₂ (red) atmosphere taken at the gold sample in 0.1 M Li₂SO₄ (pH = 3, 100 mV s⁻¹).

plotted on top of each other to facilitate comparison. The peak potentials obtained from fitting the 4-HATP/4-NSTP voltammetry (used to extract these pH data) and the current recorded at the sample during the chronoamperometry can be found in Fig. A.12 and Fig. A.13 in Appendix A. From the results in Fig. 4.3a, it can be seen that at low overpotentials and consequently low current densities (between -0.5 and -0.6 V), small pH changes of maximum 1.5 pH unit are observed at the interface, both in argon and CO₂ atmosphere. At these potentials (and pH) proton reduction is the main reaction taking place, and the activity for CO₂RR is still quite low. Although proton reduction is kinetically limited in this narrow potential window, the low proton bulk concentration (pH 3), explains the relatively small effect on the measured pH. The significant pH change we observe even when the reaction appears kinetically limited is related to the presence of the tip, which inhibits local mass transport, as we will later illustrate in the Finite Element modeling section. Between -0.65 and -0.9 V vs. Ag/AgCl, however, the pH recorded in argon atmosphere gradually increases as a function of potential. At these higher interfacial pH values, hydrogen is produced through the reduction of water. As water reduction is a kinetically limited reaction producing OH⁻, the alkalinity is expected to increase with the potential. In CO₂ atmosphere, between -0.65 and -0.8 V vs. Ag/AgCl, we observe that the pH does not significantly increase as the potential is scanned more negatively, although we work in an unbuffered electrolyte. When the pH at the interface becomes alkaline, the reversible reaction between CO₂ and

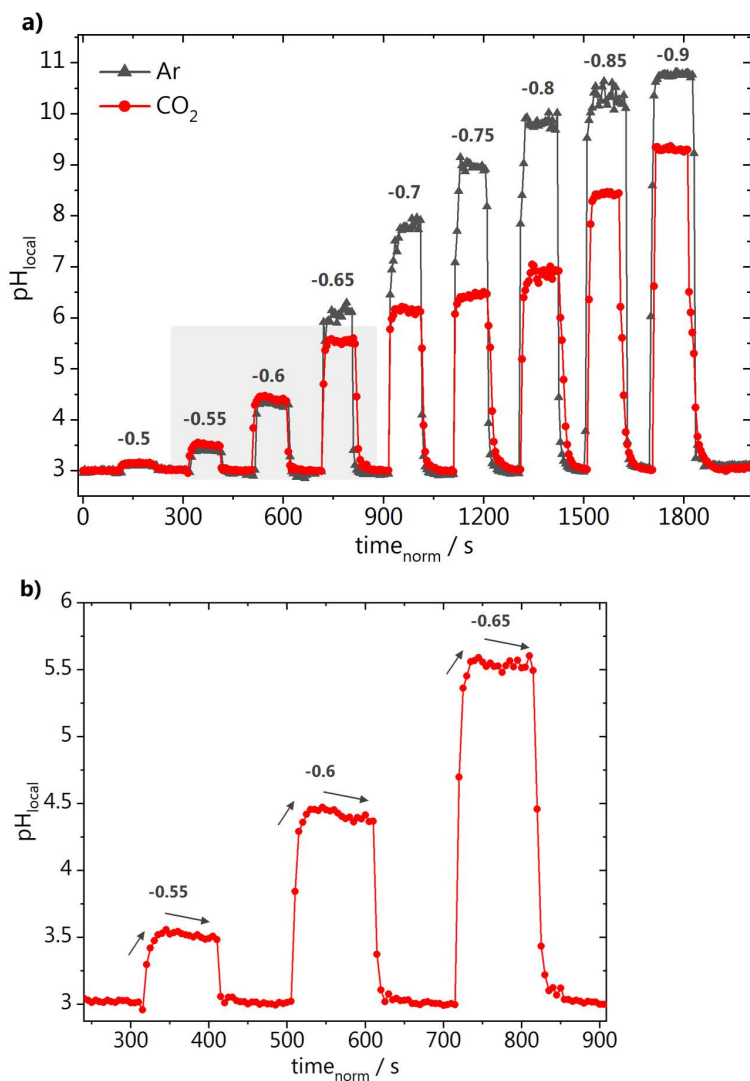


Fig. 4.3. Local pH measured in time. **a)** Comparison of the pH measured at the same distance from the surface in argon and CO_2 atmosphere; **b)** inset of the shaded area of a) showing the pH trend at low overpotentials. The sample potentials are indicated on top of the curves, in V vs. Ag/AgCl.

HCO₃⁻ (pK_a = 6.4, Eq. 4.6) seems to take place fast enough, so that the CO₂ supplied is not only a reactant but also acts as a buffer to a certain extent. Once potentials more negative than -0.8 V are applied there is a buffer "breakdown" and the pH increases more than a unit above the pK_a of the CO₂/HCO₃⁻ reversible reaction. In fact, this buffering can also be observed in CO₂ atmosphere at lower overpotentials, where the maximum pH reached is still below 6. Interestingly, as shown in Fig. 4.3b, once the reaction is turned "on", there is first an increase in pH that reaches a maximum value after 30-35 seconds. Subsequently, the pH decreases as the OH⁻ produced are neutralized by the forward CO₂/HCO₃⁻ reaction (Eq. 4.6).

Going one step further here than in Chapter 3²⁵, the dynamics of the CO₂-derived species in the diffusion layer was investigated by focusing on the relaxation of the pH after the potential is returned to 0 V, in the presence and absence of CO₂. Fig. 4.4a and Fig. 4.4b show the time evolution of the pH measured at the tip once the sample reaction is turned "off", after the different potentials shown in Fig. 4.3a are applied to the sample. It can be seen in Fig. 4.4a that in argon atmosphere, once HER is turned "off", for nearly all sample potentials the pH drops to values below 4.5 within 5 seconds. Only when the reaction is carried out at -0.9 V, it takes slightly longer, but no more than 10 seconds. For low sample overpotentials, the interfacial pH returns to bulk pH within 25 seconds and even at the higher overpotentials this takes only 35 seconds. A very different behaviour is observed in CO₂ atmosphere as a function of sample potential, and consequently local pH, as shown in Fig. 4.4b. Here, the time for returning to the bulk pH value increases gradually with the sample potential applied, which modulates the local pH and consequently the concentration of species in equilibrium in solution. At potentials more positive than -0.65 V, the pH decreases gradually and equals the bulk pH 25 seconds after the reaction is turned "off" (similarly to argon). At intermediate sample potentials (-0.7 to -0.8 V), the initial near-surface pH is above the pK_a of the CO₂/HCO₃⁻ equilibrium, and therefore the concentration of bicarbonate close to the surface is higher than in the bulk. The curves decay very similarly and for more than 15 seconds the pH stays at around 6. At the more negative sample potentials, in which carbonate is also formed in higher concentrations, the pH drops to 6 within 5 seconds, and then gradually decreases to the bulk value. These observations are a consequence of both how fast the different species formed as a function of pH diffuse in the electrolyte and the rate of the different homogeneous reactions taking place in CO₂ atmosphere. Fig. 4.4c shows a schematic representation of the reactions taking place at the sample surface and in solution. If only HER takes place

(argon atmosphere), even though the interfacial pH reaches relatively higher values, the recovery of the diffusion layer happens fast. This is a consequence of the high diffusion coefficient of the species involved in the reaction ($D_{H^+} = 9.31 \cdot 10^{-5} \text{ cm}^2 \text{ s}^{-1}$ and $D_{OH^-} = 5.27 \cdot 10^{-5} \text{ cm}^2 \text{ s}^{-1}$) and of the absence of any additional buffer system. In contrast, in CO_2 atmosphere, bicarbonate and carbonate are formed, whose concentrations are a function of pH. These are much slower diffusing species ($D_{HCO_3^-} = 1.18 \cdot 10^{-5} \text{ cm}^2 \text{ s}^{-1}$ and $D_{CO_3^{2-}} = 0.95 \cdot 10^{-5} \text{ cm}^2 \text{ s}^{-1}$).

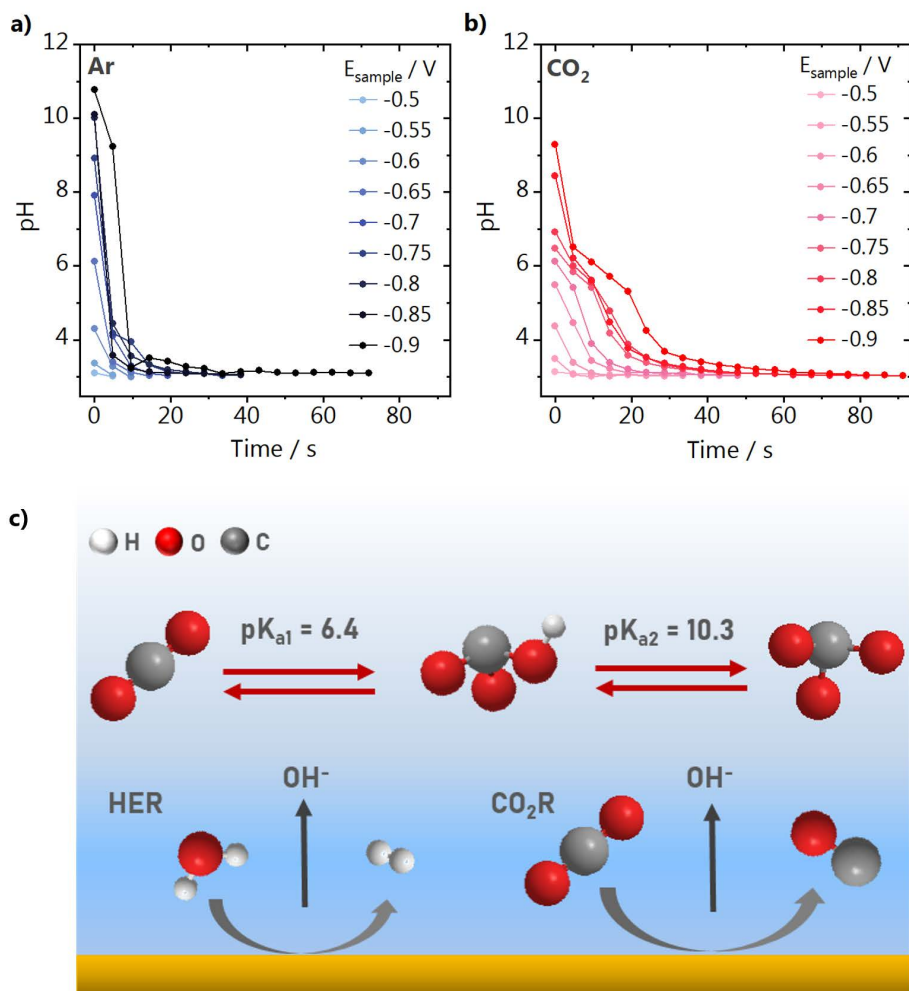


Fig. 4.4. Diffusion layer dynamics: pH recovery in the diffusion layer when **a)** hydrogen evolution and **b)** CO_2 reduction are turned "off". Sample potentials are reported versus Ag/AgCl . **c)** Schematic representation of the homogeneous reactions taking place in solution in parallel to the electrocatalytic reactions.

the reaction of $\text{CO}_3^{2-} \rightarrow \text{HCO}_3^-$ is fast while the $\text{HCO}_3^- \rightarrow \text{CO}_2$ reaction is much slower (see values in Table A.3 in Appendix A). As a consequence, the pH decays fast towards the pK_a of the $\text{CO}_2/\text{HCO}_3^-$ equilibrium, but afterwards takes more than 40 seconds to reach the bulk pH value. These observations have strong implications for experiments in electrocatalysis. For instance, if one wishes to perform several measurements in a row, enough time must be given to the system (without any reaction taking place) in order to restore the bulk pH at the interface. Furthermore, we provide here a tool for probing such equilibrium reactions under operando conditions, which is relevant not only for CO₂ reduction but also for other electrocatalytic systems.

4.4 Tip effect: Finite Element Method (FEM simulations)

In SECM it is known that the tip may physically block the diffusion of species and alter their concentrations in the diffusion layer, thus influencing the pH measurement.³² In order to account for this effect, we have simulated the experimental results presented in Fig. 4.3 (and summarized in Fig. A.14) using Finite Element Method based modelling implemented in COMSOL Multiphysics. Fitted kinetic parameters and the use of a 2D axisymmetric model leads to good agreement between simulated and experimental results. This enables us to quantify the local pH excluding the effect of the SECM tip.

First, we considered the pH response during reactions taking place in argon atmosphere (Fig. 4.3a), namely proton reduction (PR) and water reduction (WR). The governing equations as well as the parameters and the fitting procedure used to obtain these parameters are discussed in detail in Fig. A.15-18 and Table A.1-3 in Appendix A. Here, we only summarize the main points: the PR rate is assumed to be linear in the proton concentration, as is the case if the Volmer step or a large-overpotential Heyrovsky step is rate limiting. This assumption is justified by the Tafel slope obtained from chronoamperometry being 147 mV/dec (see Fig. A.15)³³ The kinetic parameters for proton reduction, as well as the proton diffusion coefficient were obtained by fitting the cyclic voltammetry (Fig. 4.2, argon), the result of which is shown in Fig A.16. Subsequently, the pH-potential relation (Fig. 4.3, argon) after 100 seconds chronoamperometry was fit to obtain kinetic parameters for water reduction. For comparison to experiment, the pH values were thereby averaged over the SECM electrode area. Relevant diffusion coefficients (except the proton diffusion coefficient) and the rate constant for water association were thereby taken from literature (see Table A.3).

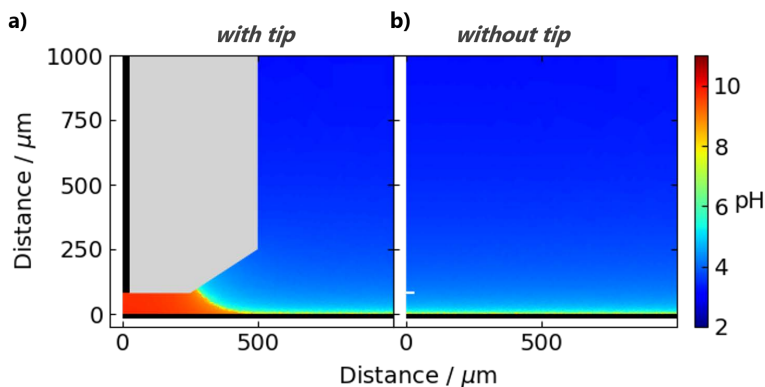


Fig. 4.5. pH profile near the electrode surface during hydrogen evolution reaction **a)** with and **b)** without the SECM tip present. Sample potential applied -0.8 V vs. Ag/AgCl.

The fitted parameters can be used to simulate the pH map during hydrogen evolution after 100 seconds chronoamperometry with and without tip present and hence to investigate the influence of the tip on the pH measurements. As an example, we show the pH map obtained at a substrate potential of -0.8 V vs. Ag/AgCl with and without the probe tip positioned at 80 μm above the surface in Fig. 4.5. The pH maps shown demonstrate that the tip significantly blocks diffusion of species away from the electrode surface. However, this effect is highly localized to the gap below the SECM tip; at horizontal positions far from the tip, the concentration profile approaches the "without tip" conditions.

Similar calculations can also be performed to estimate the influence the tip has on the transient chronoamperometry data. In Fig. 4.6, we simulate the chronoamperometry data at 100 seconds with and without tip present (solid vs. dashed line). The concentration of protons estimated with the tip absent is significantly higher than that obtained with the tip present, especially at potentials between -0.65 and -0.85 V vs. Ag/AgCl. At low overpotentials without the SECM tip present, the pH gradients are minimal. Only at large overpotentials, proton consumption at the surface electrode combined with increased hydroxide production due to the onset of water reduction causes the pH boundary layer to grow to a size comparable to the tip-surface separation (see Fig. A.18 in Appendix A). In the presence of the SECM tip, hindered diffusion directly below the tip causes the pH to rise more gradually already at a much less reducing potential. The sudden raise in pH between overpotentials of -0.6 to -0.7 V vs. Ag/AgCl can be ascribed to

a switch from proton reduction to mainly water reduction, as shown in Fig. A.17 in Appendix A.

A similar analysis was performed for the measurement in CO₂ atmosphere (Fig. 4.6b). See Eq. A.4-9 for the governing electrochemical equations and Eq. A.10-16 in Appendix A for the governing equations of the additional homogeneous reactions. Table A.3 lists the relevant parameters. Although no additional fit was performed, the simulation data (solid line) matches the experimental results (red dots) very well. Comparing Fig. 4.6a and b, it becomes clear that the pH measured in CO₂ atmosphere remains lower than that measured in argon atmosphere over the entire potential range. This is a consequence of the buffering effect of the CO₂ species present, as evidenced by the two plateau regions in the pH-potential relation, which correlate to the pK_a of bicarbonate (Eq. 4.6) and carbonate (Eq. 4.7). Although the buffering effect of the CO₂ species is most striking in the presence of the tip, the buffering of the electrolyte is also relevant in the absence of the tip. This is evidenced by the shift of the sudden increase in pH observed in argon atmosphere at -0.85V to even more negative potentials (not plotted). The presence of CO₂ and its derivatives thus has a significant buffering effect near the electrode at experimentally relevant conditions in both the presence and the absence of the tip.

Hindering the diffusion and inducing a high local alkalinity at the reaction interface allowed us to study the diffusion layer during CO₂RR at relatively low sample potentials (and current densities), which circumvents e.g. bubble issues and allows for gradually modulating the pH below the tip. However, this tip blocking effect could of course be minimized by decreasing the radius of the tip insulating layer or by working at larger distances from the surface. Using calculations similar to those shown in Fig. 4.6a, we have simulated the effect of decreasing the radius of the tip insulation on the pH response. Fig. 4.7 shows the results of the FEM simulations carried out using different insulating radii from 20*R_{tip} (the experimental value, R_{tip} from the UME used in this work) down to 1.2*R_{tip}, for a constant tip-sample distance. The simulated pH response in the absence of the SECM tip is also plotted for comparison. For an ideal insulation layer radius of 1.2*R_{tip} the calculated pH values closely approach those obtained without the tip present. When desired, this situation can be achieved, for example, by using a laser puller to produce the microelectrodes. However, it is important to point out that we find that obtaining a good sealing between the gold and the glass can be challenging, contrary to other metals that have a better adhesion to the insulation

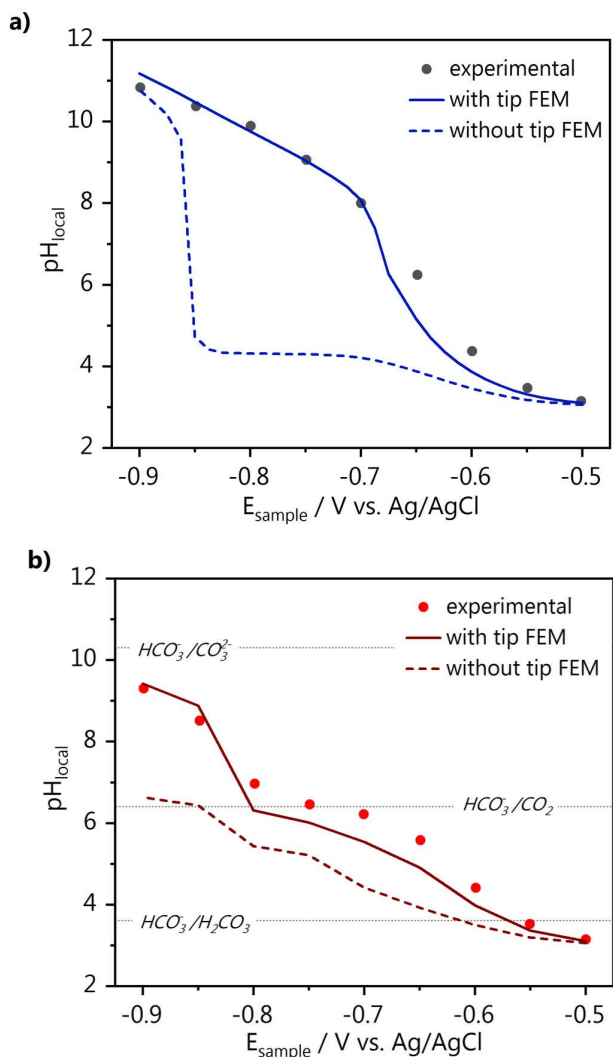


Fig. 4.6. FEM modeling of the pH response measured with SECM. **a)** Hydrogen evolution pH-potential comparison of experimental results in argon (black dots) and FEM simulation results (blue line) for $L = 3.4$ (close to the surface), compared to the case when the tip is far from the surface ($L = 50$, blue dashed line). The simulated pH "without tip" is obtained from a cross section at $80 \mu\text{m}$ from the surface with the tip removed to 1.25 mm from the surface ($L = 50$); L is the normalized tip-surface separation (see Experimental Section). **b)** Similarly, experimental (red dots) and simulation (dark red line) pH under CO_2 reduction for $L = 3.4$, is compared to simulated $L = 50$ (dark red dashed line). Bulk CO_2 concentration was fixed at 10 mM .

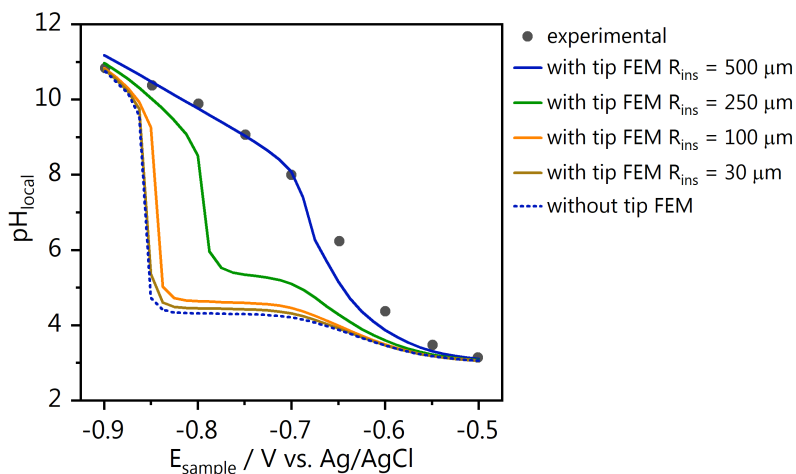


Fig. 4.7. Minimization of tip effects by decreasing the insulation radius. Comparison is made for the experiment in argon, using the results from Fig. 6a, and simulations decreasing the insulation radii, with a constant R_{tip} . The bottom tip insulation radius is maintained at $\frac{1}{2} R_{\text{ins}}$ (see Fig. A.8 in Appendix A).

layer, like platinum. Alternatively, decreasing the radius of the tip (R_{tip}) will also decrease the diffusion hindrance and change the profiles shown in Fig. 4.7.

Coupling SECM measurements with FEM simulations is a resourceful way to account for the physical blocking effect that the SECM probe has on interfacial concentration profiles. Our case is concerned with proton concentration, but the approach also applies to the detection of other species in solution, participating or not in a catalytic reaction. On the other hand, this hindrance of diffusion can also be intentionally introduced to induce a high local alkalinity in a controlled fashion, and allow the study of homogeneous and inhomogeneous reactions taking place in the diffusion layer, as shown in this and our other recent work.²⁵

4.5 Conclusions

In this Chapter, we have shown that our recently developed SECM pH sensor based on a 4-HATP/4-NSTP functionalized Au-UME is suitable for monitoring the pH in the diffusion layer during CO₂ reduction with high time resolution. We performed experiments using a polycrystalline gold substrate and monitored the pH as a function of potential at a fixed distance from the surface, in both argon and CO₂ atmospheres. Starting from bulk pH 3, we see a gradual increase in pH in argon as the potential applied is more negative, while in the presence of CO₂, a buffering

region is present, keeping the pH around the pK_a of the $\text{CO}_2 \rightleftharpoons \text{HCO}_3^-$ reversible reaction. By observing the time dependent pH decay once the reaction at the sample is turned "off" as a function of applied potential, we probe how the local pH and the rate of the homogenous reactions involving CO_2 , HCO_3^- , CO_3^{2-} influence the time required to bring the diffusion layer pH back to the bulk value. Finally, we have accounted for the effect the SECM tip has on the measured pH by performing FEM simulations. We see how the presence of the tip leads to an overestimation of the local pH, due to the hindered diffusion of species generated by the substrate. Although in this work this hindered diffusion was intentional, we also show with FEM simulations to which extent this effect can be circumvented by, for example, decreasing the radius of the tip insulation layer.

References

- (1) Kortlever, R.; Shen, J.; Schouten, K. J. P.; Calle-Vallejo, F.; Koper, M. T. M. *J. Phys. Chem. Lett.* 2015, *6* (20), 4073–4082.
- (2) Bagger, A.; Ju, W.; Varela, A. S.; Strasser, P.; Rossmeisl, J. *ChemPhysChem* 2017, *18* (22), 3266–3273.
- (3) Yu, F.; Wei, P.; Yang, Y.; Chen, Y.; Guo, L.; Peng, Z. *Nano Mater. Sci.* 2019, *1* (1), 60–69.
- (4) Vennekötter, J.-B.; Scheuermann, T.; Sengpiel, R.; Wessling, M. *J. CO₂ Util.* 2019, *32*, 202–213.
- (5) Moura de Salles Pupo, M.; Kortlever, R. *ChemPhysChem* 2019, *20* (22), 2926–2935.
- (6) Kas, R.; Kortlever, R.; Yilmaz, H.; Koper, M. T. M.; Mul, G. *ChemElectroChem* 2015, *2* (3), 354–358.
- (7) Varela, A. S.; Kroschel, M.; Reier, T.; Strasser, P. *Catal. Today* 2016, *260*, 8–13.
- (8) Marcandalli, G.; Goyal, A.; Koper, M. T. M. *ACS Catal.* 2021, 4936–4945.
- (9) Schouten, K. J. P.; Pérez Gallent, E.; Koper, M. T. M. *J. Electroanal. Chem.* 2014, *716*, 53–57.
- (10) Varela, A. S.; Kroschel, M.; Leonard, N. D.; Ju, W.; Steinberg, J.; Bagger, A.; Rossmeisl, J.; Strasser, P. *ACS Energy Lett.* 2018, *3* (4), 812–817.
- (11) Raciti, D.; Mao, M.; Park, J. H.; Wang, C. *J. Electrochem. Soc.* 2018, *165* (10), F799–F804.
- (12) Resasco, J.; Chen, L. D.; Clark, E.; Tsai, C.; Hahn, C.; Jaramillo, T. F.; Chan, K.; Bell, A. T. *J. Am. Chem. Soc.* 2017, *139* (32), 11277–11287.
- (13) Thorson, M. R.; Siil, K. I.; Kenis, P. J. A. *J. Electrochem. Soc.* 2012, *160* (1), F69–F74.
- (14) Ringe, S.; Clark, E. L.; Resasco, J.; Walton, A.; Seger, B.; Bell, A. T.; Chan, K. *Energy Environ. Sci.* 2019, *12* (10), 3001–3014.
- (15) Pérez-Gallent, E.; Marcandalli, G.; Figueiredo, M. C.; Calle-Vallejo, F.; Koper, M. T. M. *J. Am. Chem. Soc.* 2017, *139* (45), 16412–16419.
- (16) Hong, S.; Lee, S.; Kim, S.; Lee, J. K.; Lee, J. *Catal. Today* 2017, *295* (July), 82–88.
- (17) Resasco, J.; Lum, Y.; Clark, E.; Zeledon, J. Z.; Bell, A. T. *ChemElectroChem* 2018, *5* (7), 1064–1072.
- (18) Goyal, A.; Marcandalli, G.; Mints, V. A.; Koper, M. T. M. *J. Am. Chem. Soc.* 2020, *2* (1).
- (19) Schulz, K. G.; Riebesell, U.; Rost, B.; Thoms, S.; Zeebe, R. E. *Mar. Chem.* 2006, *100* (1–2), 53–65.
- (20) Monteiro, M. C. O.; Koper, M. T. M. *Curr. Opin. Electrochem.* 2021, *25* (November), 100649.
- (21) Yang, K.; Kas, R.; Smith, W. A. *J. Am. Chem. Soc.* 2019, *141* (40), 15891–15900.
- (22) Ayemoba, O.; Cuesta, A. *ACS Appl. Mater. Interfaces* 2017, *9* (33), 27377–27382.
- (23) Zhang, Z.; Melo, L.; Jansonius, R. P.; Habibzadeh, F.; Grant, E. R.; Berlinguette, C. P. *ACS Energy Lett.* 2020, *5* (10), 3101–3107.
- (24) Zhang, F.; Co, A. C. *Angew. Chemie Int. Ed.* 2020, *59* (4), 1674–1681.
- (25) Monteiro, M. C. O.; Jacobse, L.; Koper, M. T. M. *J. Phys. Chem. Lett.* 2020, *11* (22), 9708–9713.
- (26) García, G. *ChemElectroChem* 2017, *4* (3), 459–462.
- (27) Gisbert, R.; García, G.; Koper, M. T. M. *Electrochim. Acta* 2011, *56* (5), 2443–2449.
- (28) Dieckhöfer, S.; Öhl, D.; Junqueira, J. R. C.; Quast, T.; Turek, T.; Schuhmann, W. *Chem. – A Eur. J.* 2021, *27* (19), 5906–5912.
- (29) Monteiro, M. C. O.; Jacobse, L.; Touzalin, T.; Koper, M. T. M. *Anal. Chem.* 2020, *92* (2), 2237–2243.

- (30) Touzalin, T. Sorbonne Université, 2018.
- (31) Voogd, J. M. De; Spronsen, M. A. Van; Kalff, F. E.; Bryant, B.; Ostoji, O.; Haan, A. M. J. Den; Groot, I. M. N.; Oosterkamp, T. H.; Otte, A. F.; Rost, M. J. *Ultramicroscopy* 2017, *181*, 61–69.
- (32) Critelli, R. A. J.; Bertotti, M.; Torresi, R. M. *Electrochim. Acta* 2018, *292*, 511–521.
- (33) Shinagawa, T.; Garcia-Esparza, A. T.; Takanabe, K. *Sci. Rep.* 2015, *5* (1), 13801.

